Quantitative Relationships Between Microstructure and Effective Transport Properties Based on Virtual Materials Testing

Gerd Gaiselmann, Matthias Neumann, and Volker Schmidt
Institute of Stochastics, Ulm University, Ulm 89069, Germany

Omar Pecho
Institute of Computational Physics, ZHAW Winterthur, Winterthur 8400, Switzerland

Institute for Building Materials, ETH Zurich, Zurich 8093, Switzerland

Thomas Hocker and Lorenz Holzer
Institute of Computational Physics, ZHAW Winterthur, Winterthur 8400, Switzerland

DOI 10.1002/aic.14416
Published online February 25, 2014 in Wiley Online Library (wileyonlinelibrary.com)

The microstructure influence on conductive transport processes is described in terms of volume fraction ε, tortuosity τ, and constrictivity β. Virtual microstructures with different parameter constellations are produced using methods from stochastic geometry. Effective conductivities σ_{eff} are obtained from solving the diffusion equation in a finite element model. In this way, a large database is generated which is used to test expressions describing different micro–macro relationships such as Archie's law, tortuosity, and constrictivity equations. It turns out that the constrictivity equation has the highest accuracy indicating that all three parameters $(\varepsilon, \tau, \beta)$ are necessary to capture the microstructure influence correctly. The predictive capability of the constrictivity equation is improved by introducing modifications of it and using error-minimization, which leads to the following expression: $\sigma_{eff} = \sigma_0 2.03 \varepsilon^{1.57} \beta^{0.72} / \tau^2$ with intrinsic conductivity σ_0. The equation is important for future studies in, for example, batteries, fuel cells, and for transport processes in porous materials. © 2014 American Institute of Chemical Engineers *AIChE J*, 60: 1983–1999, 2014
Keywords: constrictivity, effective conductivity, electric conduction, finite element modeling, geometric tortuosity, ionic diffusion, M-factor, stochastic model

Introduction

The study of transport phenomena is a well-developed branch in physics (see e.g., Ref. 1), which is of major importance for many applied sciences such as earth science (e.g., for gas and oil exploration studies[2,3]), soil science (e.g., hydrology and contamination studies[4]), materials science (e.g., charge transport in electrodes of fuel cells and batteries[5,6]), or for chemical and biomedical engineering (e.g., transport through membranes and percolating networks of vessels[7,8]). For many engineering applications, a continuum description at macroscopic scales is often the main target. For this purpose, the effective materials properties must be well known. In this context, it is important to note that the effective transport properties are strongly influenced by morphological features at microscales such as narrow bottlenecks or tortuous pathways. Consequently, a basic understanding of the relationships between microstructure parameters and effective transport properties must be established. In the ideal case, it should be possible to predict the effective transport properties based on specific microstructure parameters.

In literature, there exist several formulas which relate volume-averaged structural parameters and effective transport properties (e.g., Refs. 5,7,9–13). Those formulas will be discussed in a separate section below. In summary, the focus of morphological characteristics relevant for transport is (a) on volume fraction ε of the transporting phase, (b) on geometric tortuosity τ, which characterizes the typical sinuousness of transport pathways, and (c) on a constrictivity parameter β, which describes the so-called bottleneck effect. Unfortunately, it is very difficult to test the validity of the proposed formulas describing the micro–macro relationship with experimental methods. The experimental limitations are partly caused by the fact that a systematic variation of the structural parameters results in a very large number of samples. Such a large testing matrix cannot be analyzed with reasonable experimental resources. In addition, the available fabrication techniques generally do not allow varying the microstructure parameters independently from each other and over a large range.

An alternative approach to test the formulas for a micro–macro relationship is based on the application of microscale

Correspondence concerning this article should be addressed to G. Gaiselmann at gerd.gaiselmann@uni-ulm.de.

transport models (micromodels), which are suitable to study microstructure effects. For this purpose, Lattice Boltzmann modeling (LBM)[14–16] or finite element modeling (FEM),[17] respectively, can be used to solve transport equations based on a structural grid. This grid, which represents the three-dimensional (3-D) morphological details of the microstructure, can be obtained by transformation of 3-D-data from high-resolution tomography.[18,19] In this way, the micromodels provide a direct link between the microstructure, which is intrinsically represented by the grid, and the effective transport properties, which result from the simulation itself. Consequently, the micromodels can be used to empirically establish quantitative relationships between effective transport properties (e.g., effective electric conductivity σ_{eff}) and corresponding microstructure parameters (ε, τ, β). The latter parameters are determined by 3-D image analysis from the tomographs, as demonstrated in earlier studies.[2,5,6,20–22] A major drawback of transport studies based on micromodels is the limited number of samples that can be analyzed, as the simulation requires extensive computational resources. In addition, when tomographs from real materials are used as a basis for the simulations, then the problem of a limited structural variation arises, similar to the limitations mentioned above for the experimental studies. Due to these limitations in experimental and modeling studies, the quantitative relationships between microstructure parameters and effective macroscopic transport properties are not yet established in a conclusive way.

For this study, we thus propose a different methodological approach, which enables testing of proposed formulas from literature based on a larger range of samples and microstructures, respectively. Thereby, we investigate the transport properties of virtual 3-D microstructures that are generated with methods from stochastic geometry.[23,24] In earlier studies, it was proven that such stochastic models are capable to precisely describe the topology of advanced energy materials such as electrodes for fuel cells and batteries.[21,25,26]

A stochastic modeling approach is used to produce a set of virtual microstructures with varying constellations of structural characteristics (ε, τ, β). The corresponding transport properties are determined with FE-simulations. This virtual materials testing (VMT) approach provides a statistically sound analysis of the quantitative relationships between the structural parameters and the effective transport properties.

In the following sections, we will give a detailed introduction to the topic. We first define the transport mechanisms and corresponding effective transport properties for which the established relationships are considered to be valid. Subsequently, we introduce the basic microstructural characteristics, which have a critical influence on effective transport properties according to literature. Then, the most widely used empirical relationships between effective transport properties and structural characteristics are briefly reviewed. An important part of the article is dealing with the methodologies for VMT by stochastic modeling and FEM. The formulas from literature are then evaluated on the basis of our results from VMT. The results are compared with experimental data from a Ni-cermet anode for solid oxide fuel cells (SOFC). Based on our results, a refined formula for micro–macro relationships can be proposed, which has a more general meaning than the existing formulas in literature, due to the extensive set of microstructural data, on which it is based.

Transport processes and effective transport properties

In this study, we consider effective transport properties of composite materials, where transport takes place only in one phase and the other phase(s) is (are) not conducting. An example is the electric conductivity in a porous Ni-YSZ anode for SOFC, where electric transport takes place only in the nickel-phase. The electric charge transport is described by Ohm's law

$$J = -\sigma \frac{dU}{dx} \tag{1}$$

and

$$\frac{dU}{dt} = \sigma \frac{d^2U}{dx^2} \tag{2}$$

where J is the current density, σ is the conductivity, U is the electric potential, and t is time. With constant boundary conditions, such systems tend to approach a steady state, which is described by the Laplace equation

$$\frac{d^2U}{dx^2} + \frac{d^2U}{dy^2} + \frac{d^2U}{dz^2} = 0 \tag{3}$$

where x, y, and z are the space coordinates. In principle, an analogy can be drawn to transport processes, which obey the same mathematical description (e.g., diffusive mass transport by Fick's law or heat diffusion). For a detailed discussion, see Ref. 1. The influence of the microstructure on the macroscopic behavior described in (1) and (2) is introduced with a microstructure-factor (M-factor), as follows

$$\sigma_{\text{eff}} = \sigma_0 M \tag{4}$$

Here, σ_{eff} is the effective conductivity, σ_0 is the intrinsic conductivity (i.e., without geometric constraints), and M is a correction factor, which describes the transport limitations caused by microstructure effects. The aim of this study is to find quantitative expressions for the M-factor in terms of phase volume fraction (ε), tortuosity (τ), and constrictivity (β) with the aid of FE simulation of electrical conduction. Based on the concept of analogy, the same expressions should in principle also be applicable for a description of microstructure effects in systems with mass transport by diffusion or energy transport by heat conduction. However, it has to be emphasized that our considerations of microstructure effects are limited to the rather basic cases where transport takes place in only one phase of the composite material. Furthermore, our considerations also do not include transport processes that require a different mathematical treatment such as advective, radiative, or reactive transport and any kind of flow (viscous, turbulent). Additional limitations for the validity of the established micro–macro relationships occur for systems where the interaction between phase boundary and transported species becomes important due to physisorption and chemisorption. This is usually the case for very fine microstructures (e.g., nanoporous samples) and for materials with a relatively high surface potential on the pore wall, see, for example, Ref. 27.

Microstructure parameters relevant for transport

In this section, we summarize the definitions and principles of image processing, which are required for quantitative analysis of the transport relevant parameters.[28–30] These parameters include volume fraction of the transporting phase

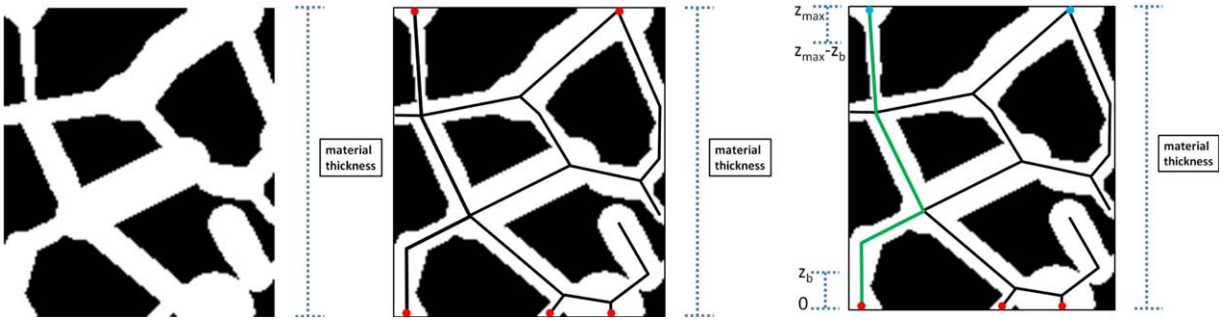

Figure 1. Basic idea of geometric tortuosity τ explained on a 2-D example: material with white colored phase of interest (left), extraction of graph (center), and computation of shortest paths (green line, right) from a chosen inlet-point (red circle, right) to the corresponding outlet-points (blue circles, right).

The geometric tortuosity τ is then given by the mean length of shortest paths ℓ_e divided by the material thickness ℓ. [Color figure can be viewed in the online issue, which is available at wileyonlinelibrary.com.]

ε, geometric tortuosity τ, and constrictivity β. For the characterization of the volume averaged parameters, let us assume that the material under consideration consists of several phases and it is given on a finite observation window $W=[0, x_{\max}]\times[0, y_{\max}]\times[0, z_{\max}]$ with volume v_W. The volume fraction of the phase of interest ε is then defined by the ratio of the volume of this phase v_I divided by the total volume of the observation window v_W, that is, $\varepsilon=v_I/v_W$.

The microstructure parameter tortuosity is often considered as a major morphological parameter, which potentially controls the macroscopic transport properties. However, there is confusion about the tortuosity concept, because there exist many different definitions and different measurement techniques for it (see e.g., Ref. 13). In this study, we concentrate on the "geometric tortuosity" τ, which is defined as the ratio of the mean shortest transport path length ℓ_e divided by the direct length of sample thickness ℓ, that is, $\tau=\ell_e/\ell$. To determine the geometric tortuosity, the mean shortest paths length ℓ_e is computed based on 3-D image data, for example, from tomography, see Figure 1. In particular, the phase of interest of this 3-D image is first transformed into a 3-D graph; see Figure 1 (center). In our case, the 3-D graph is computed using the skeletonization algorithm implemented in the software Avizo 7.[31] Within this graph, we define inlet-points (bottom) and outlet-points (top), see Figure 1 (center). In terms of the so-called "geometric tortuosity," for each inlet-point only the path is selected, which has a minimum length to one of the outlet-points, see Figure 1 (right). The mean value of all these shortest path lengths is considered as the mean shortest paths length ℓ_e. An algorithm for the identification of shortest pathways from complex 3-D graphs is described in Ref. 32. Note that the inlet-points for the calculation of shortest paths are the vertices $v=(v_x, v_y, v_z)^\top$ of the graph located at the bottom, that is, $v_z \in [0, z_b]$, and correspondingly for the outlet-points at the top, that is, $v_z \in [z_{\max}-z_b, z_{\max}]$). Thereby, $z_b > 0$ is chosen so that the graph contains more than hundred inlet- and outlet-points, respectively, in order to obtain a sufficiently large number of shortest pathways for estimating τ.

In the next step, we present a volume-averaged structural parameter β characterizing the "constrictivity" of a microstructure. Note that β is a quantitative description of bottleneck effects (i.e., constrictivity) in complex microstructures. It has been introduced in Ref. 5 as the ratio of minimum cross-section (bottleneck) over maximum cross-section (bulge). This expression reduces to $\beta=(r_{\min}/r_{\max})^2$ where $r_{\min}$ indicates the radius of "characteristic bottleneck median" and $r_{\max}$ the radius of phase size median. To compute $r_{\min}$ and $r_{\max}$ from a 3-D microstructure, the concept of the continuous phase size distribution (cPSD) and a computational tool mercury intrusion porosimetry-PSD (MIP-PSD), which allow the simulation of MIP are needed, compare Ref. 20. The cPSD $P(r)$ describes the volume fraction of the phase of interest, which can potentially be covered by spheres with radii r where the spheres have to be completely located in this phase. The parameter $r_{\max}$ is defined by $r_{\max}=P^{-1}(0.5)$ being the radius r of the cPSD $P(r)$ filling 50% of solid volume v_S, see Figure 2. Thus, $r_{\max}$ can be regarded as the radius of the phase size median. MIP is an experimental technique to characterize the pore-size distribution in porous materials. The MIP measurements are strongly influenced by narrow constrictions along the intrusion pathways. Therefore, the characteristic peak in MIP-PSD, which is also called "break-through radius," is considered as being equivalent with the characteristic size of the bottlenecks. In our

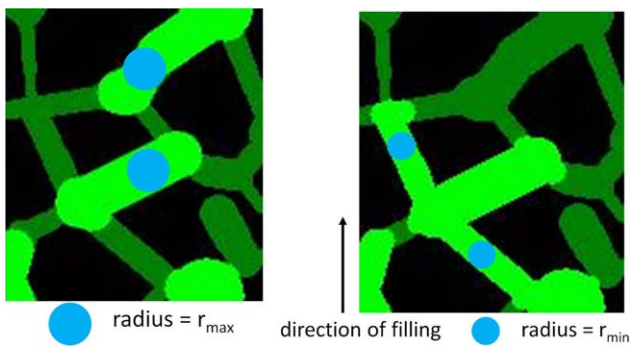

Figure 2. Left: determination of r_{max} by cPSD.

The radius of the blue sphere is determined as r_{max}, when 50% of the phase of interest (bright green area) can be covered by union of spheres (blue) with radii r_{max}; right: determination of r_{min} by MIP-PSD. The radius of the blue sphere is determined as r_{min}, when 50% of the phase of interest (bright green area) can be covered by union of spheres (blue) with radii r_{min}, but with the important restriction of a directed filling from the bottom. Note that this union of spheres is always connected to the bottom. [Color figure can be viewed in the online issue, which is available at wileyonlinelibrary.com.]

image analysis approach, the concept of the MIP-PSD is closely leaned on that of the cPSD, in the sense that both methods are based on the same type of Euclidean distance map. However, for the MIP-PSD additional constraints are introduced to simulate the intrusion of mercury from the bottom of the sampling window to the top. The basic idea is to consider a "directed filling" of the phase of interest by spheres. More precisely, those regions of the phase of interest are filled, which can be reached by a sphere with radius r, starting, for example, from the bottom of the material. Thereby, the sphere is not allowed to intersect other phases. We denote the volume fraction of these regions by $M(r)$. The parameter $r_{\min}$ is defined by $r_{\min}=M^{-1}(0.5)$. It can be considered as the radius of the characteristic bottleneck median, see Figure 2. For further information about the cPSD, MIP-PSD, and constrictivity β, the reader is referred to Refs. 5,20.

Empirical relationships describing microstructure influence on the effective transport properties

The three parameters introduced in the previous section (ε, τ, and β) appear in different expressions, which are discussed in literature to describe the microstructure effect M of Eq. 4. These expressions are briefly reviewed in this section.

Transport properties of porous sediments are intensively investigated in geoscience in the context of oil and gas exploration which led to the postulation of an exponential relationship known as Archie's law[9]

$$M=\varepsilon^m \tag{5}$$

where $m \in \mathbb{R}$ is a constant that is characteristic for each type of sedimentary rock. However, the exponent m cannot be explained in terms of any specific topological or morphological feature. Therefore, Archie's law does not really help to fundamentally understand the influence of microstructure on the transport properties.

The concept of tortuosity τ was first introduced in Ref. 12 and later refined in Ref. 11. This concept states that the length of transport pathways has a significant influence on the effective transport properties. In literature (e.g., Ref. 33), this is usually expressed as follows

$$M=\frac{\varepsilon}{\tau^2} \tag{6}$$

Note that throughout the article, we call this expression the "tortuosity equation." Unfortunately, there exists no unique definition of τ in literature, compare Ref. 13 for a detailed discussion. Many authors do not apply the concept of the geometric tortuosity for τ as introduced in the previous section. Instead, the tortuosity can be indirectly computed by (physically) measuring D_{eff}, D_0, and ε and solving Eq. 6 with respect to τ, called experimental tortuosity τ_{exp}. Alternatively, the tortuosity can be simulated (e.g., by FEM or LBM), called effective tortuosity τ_{eff}. In both cases, τ_{exp} and τ_{eff}, unrealistically high values are often achieved for tortuosity (i.e., up to 10 and even higher).[33–36] Geometric models show that such long pathways are not realistic (e.g., Refs. 33–37). In a recent study,[7] geometric and experimental tortuosities were determined for porous membranes covering a large range of porosities (i.e., $\varepsilon \in [0.3, 0.8]$). It turned out that the experimental tortuosities vary from 1.0 up to larger than 5.0, whereas the geometric tortuosities in the same samples exhibit very similar values between 1.5 and 1.7. These results indicate that experimental tortuosity tends to include additional microstructure effects other than the tortuous pathways. As a consequence, we restrict our consideration of tortuosity τ in this study exclusively to the notion of geometric tortuosity. The apparently high values for experimental tortuosities could be explained by the fact that it includes the influence from narrow bottlenecks. Thus, the concept of tortuosity given in (6) was then combined with the consideration of bottleneck effects which led to the following expression (see e.g., Ref. 10)

$$M=\frac{\varepsilon\beta}{\tau^2} \tag{7}$$

Note that throughout the article, we call this expression the "constrictivity equation." A major problem for the practical use of the constrictivity equation was the fact that there were no techniques available for measuring the constrictivity in real samples. Obviously, this is the reason why in many experimental studies all microstructure effects are assigned to the (experimental) tortuosity. However, recently a new methodology for measuring constrictivity has been introduced with image processing techniques based on cPSD and MIP-PSD,[5,20] as summarized in the previous section. The significance of this methodology is the fact that it can be applied to 3-D data from real samples with disordered microstructures. This opens new possibilities to distinguish microstructure effects originating from narrow bottlenecks and from tortuous pathways.

Methods—Towards a VMT Laboratory

In the previous section, the most widely used empirical relationships have been introduced relating structural characteristics and the corresponding effective materials properties. To evaluate the predictive capabilities of these formulas, we introduce a VMT approach. More precisely, a stochastic simulation model produces microstructures with predefined structural characteristics ε, τ, and β. On these synthetic microstructures, the effective transport properties and the M-factors are computed by means of FE simulations. This database is then used to systematically analyze the relationships between structural characteristics and the effective material properties in an empirical way.

Stochastic 3-D microstructure model

In this section, a stochastic simulation model is introduced, which generates two-phased 3-D microstructures with a large spectrum of three structural characteristics, ε, τ, and β. Simulations drawn from the stochastic model are realistic representations of real microstructures as, for example, anodes of SOFC. The construction of such a stochastic model which simulates microstructures with independently varied structural parameters is challenging because it is natural that a high volume fraction (≈ 1), for example, leads to a low tortuosity (≈ 1). Contrarily, if the volume fraction tends to zero then the constriction factor is typically low (≈ 0) and the tortuosity tends to increase.

Our basic idea for the construction of the stochastic microstructure model is as follows. In the first step, a random geometric graph $G=(V,E)$ is introduced where $V=\{V_1, V_2, \ldots\}$ represents the set of vertices and $E=\{(V_{i_1}, V_{j_1}), (V_{i_2}, V_{j_2}), \ldots\}$ the set of edges, which describes the line segments connecting two vertices. This graph determines the main

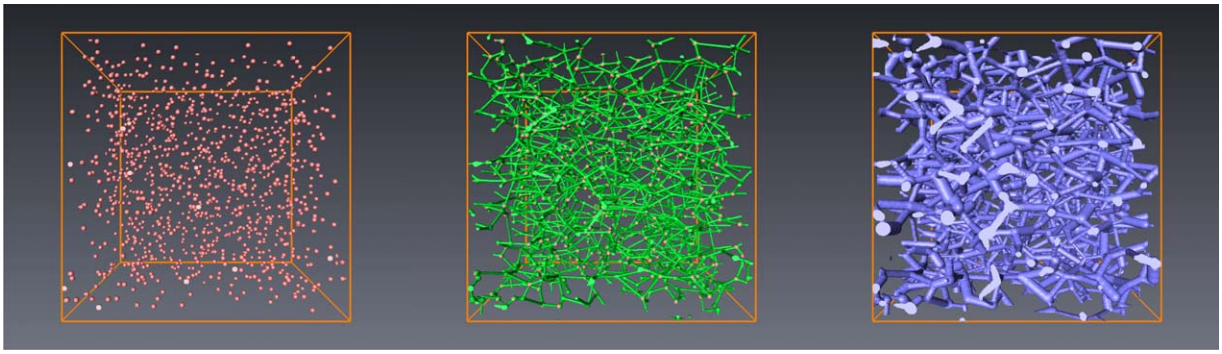

Figure 3. Basic idea of the stochastic microstructure model: modeling of vertices by a 3-D point process (left), introducing edges (center), and dilation of edges by independent random radii (right).

[Color figure can be viewed in the online issue, which is available at wileyonlinelibrary.com.]

morphological features of the structure. The vertex set V of the graph G follows a random 3-D point process, compare Figure 3 (left). Moreover, the edges connecting the vertices V are set such that the graph G is completely connected (with probability 1) and the direction distribution of edges (anisotropy of edge directions) can be nicely controlled, see Figure 3 (center). Note that in this way, the (geometric) tortuosity of the graph can be controlled, too. Finally, all edges are dilated in 3-D with independent random radii following some distribution, compare Figure 3 (right). Thereby, the radius of the solid phase median $r_{\max}$ and the bottleneck radius median $r_{\min}$ can be regulated and in this way, the constrictivity β can be controlled. As the stochastic microstructure model is constructed by a random graph, we call it a stochastic spatial graph model (SSGM).

Stochastic Modeling of Spatial 3-D Graph. The random spatial 3-D graph is constructed by a two-stage approach. First, the vertex set V of the graph G is described by a homogeneous 3-D Poisson point process[24] with some intensity $\lambda > 0$. A Poisson point process realized in a bounded observation window W consists of a Poisson distributed number of points with expectation λv_W depending on the intensity λ and the volume of the observation window v_W, where the points are independently sampled and uniformly distributed in W.

In a second step, the set of edges E given the vertex set V is modeled by a modified version of the relative neighborhood graph (RNG).[38] The RNG defines an undirected graph on a set of points (i.e., in our case on $V=\{V_1, V_2, \ldots\}$) where two points V_i and V_j are connected by an edge whenever there does not exist a third point V_k (for all $k \notin \{i,j\}$) that is closer (with respect to the Euclidean distance d) to both V_i and V_j than they are to each other, that is, $d(V_i,V_j) \leq \max\{d(V_i,V_k), d(V_j,V_k)\}$ for all $k \notin \{i,j\}$, see Figure 4. Note that the RNG is completely connected if the set of vertices V is finite or V is described by a class of point processes following some regularity conditions (see Ref. 38 for more details), as the Poisson point process does. For isotropic point patterns V, the RNG yields an isotropic edge set.

Besides the creation of a completely connected graph G embedded in the 3-D space, we aim to control the tortuosity of the graph by including anisotropy to the set of edges. Thus, the RNG is modified by substituting the Euclidean distance d in the definition of the RNG by another distance measure d_α, that is given by

$$d_\alpha(V_i,V_j) = d(V_i,V_j)\max\left\{0.01, \left(1-\frac{2\varphi(V_i,V_j)}{\pi}\right)\right\}^\alpha$$

where $\varphi(V_i,V_j) = \min\left\{\measuredangle\left(V_i-V_j, (0,0,1)^\top\right), \measuredangle\left(V_i-V_j, (0,0,-1)^\top\right)\right\}$ denotes the acute angle between the line segments V_i-V_j and $(0,0,1)^\top$. Following the argument provided in Ref. 38, it can be shown that the resulting graph is completely connected on V for each $\alpha \in \mathbb{R}$, because $0 \leq 2\varphi(\cdot,\cdot) \leq \pi$ and thus $\max\left\{0.01, \left(1-\frac{2\varphi(V_i,V_j)}{\pi}\right)\right\}^\alpha$ is bounded on both sides.

Note that the parameter α of the modified RNG (mRNG) controls the anisotropy of the edge set E with respect to the z-direction (i.e., $(0,0,1)^\top$ direction). In the case that $\alpha < 0$ ($\alpha > 0$), the distance $d_\alpha(V_i,V_j)$ between two vertices V_i and V_j becomes small (large) if the acute angle $\varphi(V_i,V_j)$ is small. Thus, for $\alpha < 0$ ($\alpha > 0$), pairs of vertices (V_i,V_j) having a small (large) acute angle to $(0,0,1)^\top$ are preferred to be connected in the mRNG. In other words, for $\alpha < 0$ ($\alpha > 0$), vertically (horizontally) oriented edges are preferred, see Figure 5 (left and right, respectively).

For both cases (i.e., $\alpha < 0$ and $\alpha > 0$), the dependence between the values of $d_\alpha(V_i,V_j)$ and $\varphi(V_i,V_j)$ becomes stronger for a larger absolute value of α. If $\alpha=0$, the mRNG coincides with the classical RNG and thus the directional distribution of edges is isotropic if the underlying point process is isotropic too, see Figure 5 (center). Note that the

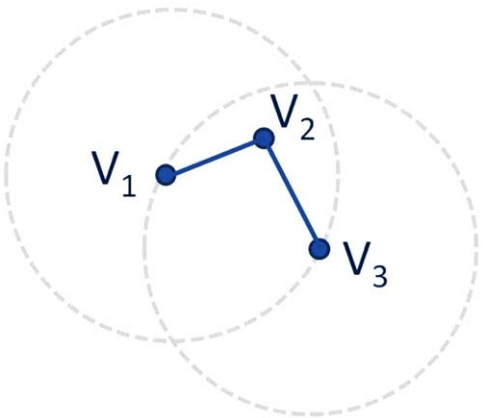

Figure 4. RNG of the set of vertices V_1, V_2, V_3.

[Color figure can be viewed in the online issue, which is available at wileyonlinelibrary.com.]

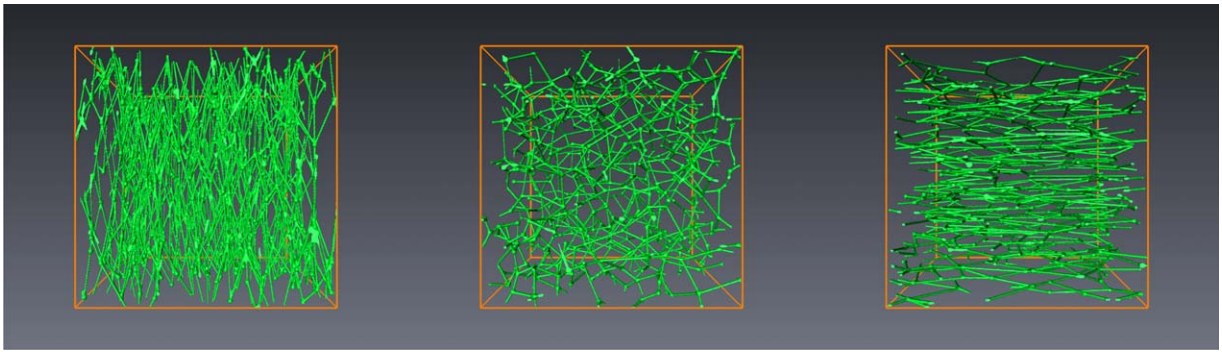

Figure 5. Realizations of the mRNG with fixed intensity $\lambda=4.63\times10^{-6}$ of vertices and with $\alpha=-5$ (left, vertically orientated edges); $\alpha=0$ (center, isotropic directions of edges), and $\alpha=5$ (right, horizontally orientated edges).

[Color figure can be viewed in the online issue, which is available at wileyonlinelibrary.com.]

spatial graph model $G=(V,E)$ is uniquely described by the parameters λ and α.

Local Dilation of Edges. So far, the spatial 3-D graph model introduced in the previous section consists of an ensemble of random line segments. From a mathematical point of view, the 3-D volume of this arrangement of line segments is equal to zero. Therefore, to complete the stochastic microstructure model, we dilate each edge of the spatial graph model G with a sphere as structuring element where the radius of the sphere is random. More precisely, each edge E_i is assigned an independent and identically distributed random radius R_i following a shifted Gamma distribution, where the Gamma distribution, uniquely described by their mean value $g_1 > 0$ and variance $g_2 > 0$, is shifted by 1 to the right. To shift the Γ-distributed radii by 1 is reasonable to ensure that the dilation radius of the edges is larger than the voxel resolution since otherwise the edge could not be displayed when discretizing the microstructures to a 3-D image. Subsequently, each edge E_i of the graph G is dilated with the sphere $b(0,R_i)$ as structuring element with origin as center point and radius R_i, see Refs. 29,30. Note that the dilated graph defines the SSGM. Realizations drawn from the SSGM are visualized in Figure 6. Also, note that the dilation of edges has an significant influence on the structural characteristics ε, τ, and β. The (geometric) tortuosity τ is mainly determined by the anisotropy parameter α of the graph model G, but when dilating the edges of the graph by spheres with large radii it may occur that neighboring edges overlap. In this case, the extracted graph for the computation of the tortuosity τ consists of different edges as G which may lead to a significant decrease of τ in comparison to the tortuosity computed for the (nondilated) graph G. In summary, we have chosen the parameters (λ,α,g_1,g_2) of the SSGM such that we are in the position to obtain a wide spectrum of volume fractions ε, tortuosities τ, and constriction factors β.

Single tube with random hyperbolic bottlenecks

As discussed earlier, there is evidence from experimental studies[7] that the variation of geometric tortuosity in real samples is very limited (ca. 1.5–2.0). This indicates that the large variation of the experimental tortuosity (between 1.3 and 10!) reported in literature,[13] does not reflect true variations of the path lengths but instead it is related to other microstructure effects such as the influence of narrow bottlenecks. To study this bottleneck effect without any influence of geometric tortuosity, we have thus developed a so-called hyperbolic bottleneck model (HBM). It consists of a single tube with sequences of hyperbolic bottlenecks. More precisely, the HBM generates 3-D microstructures by rotation of two-dimensional (2-D) microstructures realized on a rectangle with hyperbolic bottlenecks, see Figure 7. Thus, geometric tortuosity τ is fixed at 1 as the shortest pathways are described by a single straight line segment running through the center of the tube. This allows us to analyze the specific influence of β and ε on effective transport properties while keeping τ constant. Furthermore, FE simulations based on structures with rotation symmetry can be done in a very time-saving way.

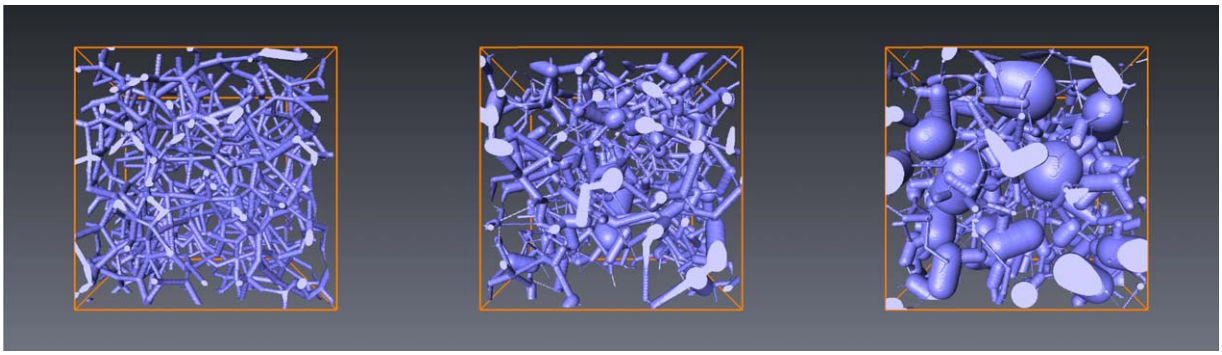

Figure 6. Realizations drawn from the SSGM with different degrees of dilation.

All three structures have the following identical parameters $(\lambda=4.63\times10^{-6}, \alpha=0, g_1=5)$ but g_2 is varied, that is, $g_2 = 1$ (left), $g_2 = 4$ (center), and $g_2 = 7$ (right). [Color figure can be viewed in the online issue, which is available at wileyonlinelibrary.com.]

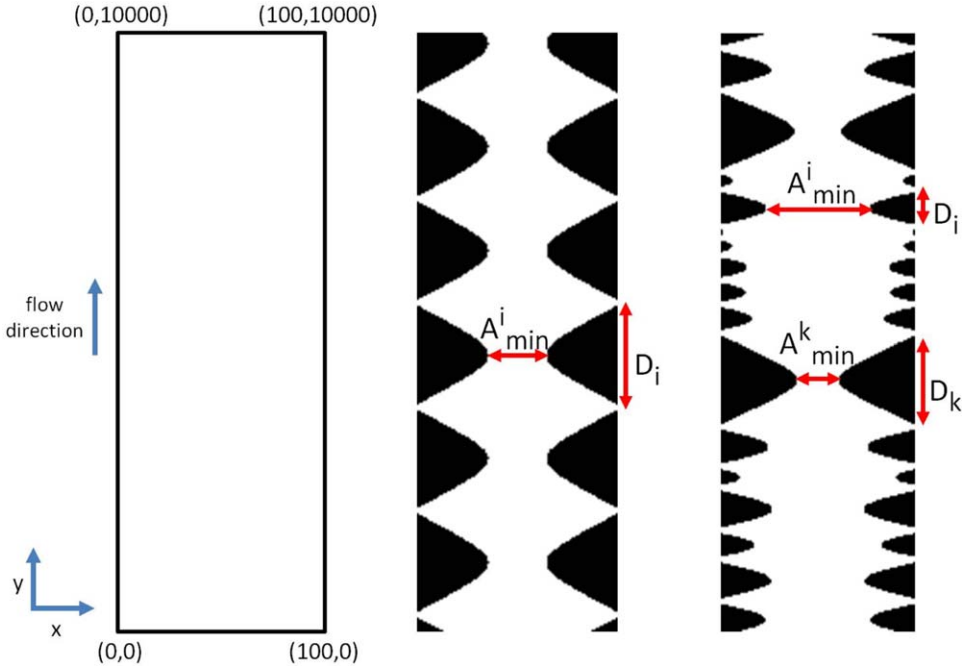

Figure 7. Illustration of the HBM.

3-D tubes with rotational symmetry are created from a single 2-D tube with sequences of hyperbolic bottlenecks. The radii of and the distances between bottlenecks are chosen either deterministically (center) or at random (right). [Color figure can be viewed in the online issue, which is available at wileyonlinelibrary.com.]

For construction of the HBM, we restrict the observation window to a rectangle with width 100 and length 10,000, that is, $[0,100]\times[0,10,000]$ (see Figure 7, left). To this rectangle (two-dimensional (2-D) tube), a sequence of hyperbolic bottlenecks is added where the diameters of the hyperbolic bottlenecks (the diameter of the constrictions) are chosen by a sequence of independent and uniformly distributed random variables $A_{\min}=\{A^1_{\min},A^2_{\min},\ldots\}$, where $A^i_{\min} \sim U[r_1,r_2]$ with $0\le r_1\le r_2\le 100$ and $i\in\mathbb{N}$. Furthermore, the sequence of distances $\{D_1,D_2,\ldots\}$ between bottlenecks depends on $A_{\min}$ and a further parameter d_m, where for each $i\in\mathbb{N}$ it holds that $D_i=(A^i_{\min}/d_m)\tan(\operatorname{acos}(A^i_{\min}/100))$ (Figure 7, center and right). Note that the sequence of bottlenecks can be chosen in a deterministic way if we set $r_1=r_2$. By the choice of these three model parameters, the volume fraction ε and the constrictivity parameter β are controlled, whereas the tortuosity τ is equal to 1.

Experimental analysis of Ni-cermet anodes for SOFC

The relationship between 3-D-microstructure and effective electrical conductivity is experimentally investigated for the Ni-phase in composite Ni-YSZ anodes of SOFC. Thereby, the anode material is considered in its initial state (after the first reduction) and in a degraded state after exposure to eight redox-cycles. Hence, the experimental investigations include fabrication of the anode samples, degradation test by exposure to eight redox-cycles, and measurement of electrical conductivity, see Ref. 39 for further information. Electrical conductivity is characterized with four-point measurements for the initial state and for a degraded state after eight redox-cycles.

As a result, it was found that the electric conductivity σ_{eff} in the anode material is dropping from 600 S/cm (initial state) to 200 S/cm (after redox). The microstructure effects, that is, the M-factors, can be calculated by substituting the measured effective conductivities σ_{eff} and the known intrinsic electrical conductivities σ_0 into Eq. 4, which are subsequently termed M_{meas}. With $\sigma_0=22,100$ S/cm (at 950°C) we obtain $M_{\text{meas}}=0.027$ for the initial state and $M_{\text{meas}}=0.0095$ for the anode exposed to eight redox-cycles. Hence, the microstructure effect is much more limiting for electrical current in the anode, which suffered degradation compared to the anode in the initial state.

In another previous study, we have characterized the 3-D microstructure of the porous Ni-YSZ anode samples by focused ion beam (FIB)-tomography. For a detailed description of the imaging and image analysis techniques, we refer to Ref. 6. The nickel phase, which conducts electrical current through the anode, undergoes significant morphological changes due to the redox exposure, see Figure 8. The nickel degradation is dominated by grain growth (i.e., coarsening) and loss of connectivity (i.e., formation of isolated grains). In particular, the nickel volume fraction is decreasing from $\varepsilon_{\text{before}}=0.317$ to $\varepsilon_{\text{after}}=0.180$, which is due to the loss of connectivity (i.e., isolated grains are excluded from the effective nickel volume fraction). Also, the constrictivity is decreasing from $\beta_{\text{before}}=0.291$ to $\beta_{\text{after}}=0.188$. In contrast, geometric tortuosity remains nearly constant with $\tau_{\text{before}}=1.726$ and $\tau_{\text{after}}=1.765$ (see also Table 3).

Finite element computation of effective transport properties

For computation of transport properties, we use SESES, which is an in-house FE code for multiphysics simulation developed at Zurich University of Applied Sciences, see Ref. 40. The effective electrical conductivity is evaluated in SESES by applying an external potential difference and by solving for the resulting current densities via ohms law. In our simulations, we assign an intrinsic conductivity of 1 S/cm to the conducting phase. In this case, the M-factor coincides with the computed effective conductivity,

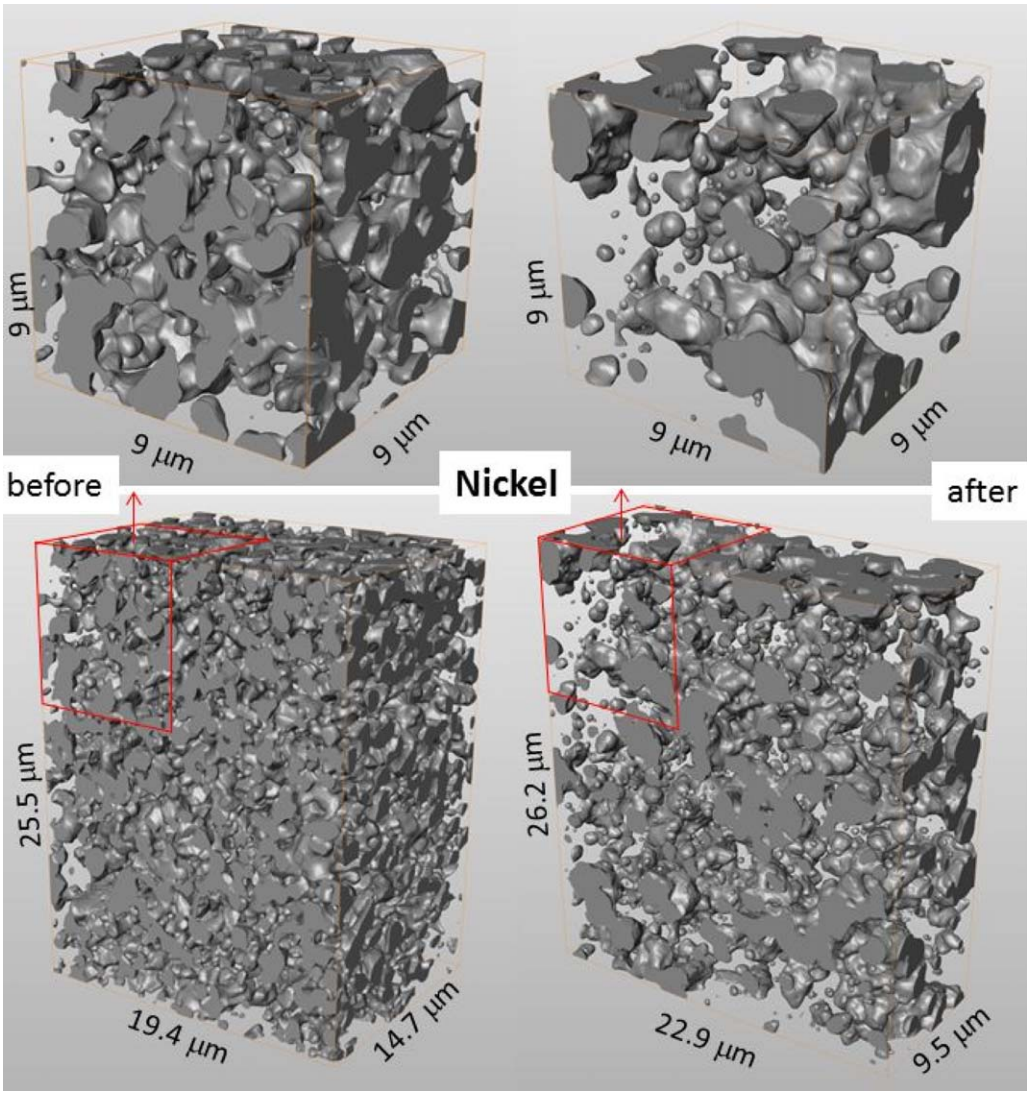

Figure 8. Illustration of the nickel morphology in Ni-YSZ anodes before (left) and after (right) redox cycling.

Due to the degradation, the nickel phase is coarsening and some grains are forming isolated islands, which do not contribute to the transport of electrical current (Reproduced from Ref. 6). [Color figure can be viewed in the online issue, which is available at wileyonlinelibrary.com.]

see Ref. 3. FE simulations are performed based on 3-D grid representations. For FE simulations based on SSGM structures, we create meshed grids based on data cubes of 500×500×500 voxels (resolution 20 nm). For FE simulations with real SOFC anodes, we crop cubes of 400×400×400 voxels (resolution 20 nm) from the segmented FIB data. When the grids from SSGM are reproduced with the same stochastic input parameters, then reproducibility of the structural parameters (ε, τ, and β) is within 2%. The good reproducibility also shows that the cube size region of interest (ROI) is representative. For the transformation of voxel-based data into meshed grids, we use Avizo software, see Ref. 31. On the left side of Figure 9, the surface of the nickel phase in the anode (before redox) is shown. This surface is represented by 0.310^6 faces and the 3-D grid is represented by 10^6 tetrahedrons. Figure 9 (right) represents a virtual microstructure from SSGM, which has the same morphological characteristics as the nickel phase from FIB-tomography (before redox) in terms of volume fraction (ε), tortuosity (τ), and constrictivity (β). It is also represented with a similar resolution (i.e., surface: 0.310^6 faces; 3-D grid: 10^6 tetrahedrons). According to the hypothesis of this work, the microstructure influence on transport properties is fully described by ε, τ, and β. Consequently, the FE simulations of the two structures from real anode and from SSGM in Figure 9 should provide the same effective transport properties (see Figure 9 and the discussion thereof).

FE simulations are also performed on single tubes with rotational symmetry from HBM. For this geometrical setup, we perform pseudo 3-D transport simulations, which are based on 2-D pixel-images representing the tubes with hyperbolic constrictions, and applying corrections for the 3-D rotational case. These simulations are much more efficient than the calculations based on complex 3-D-meshes and thus the full pixel image resolution can be maintained. The physics (i.e., Ohms law, external potential as a driving force, intrinsic material properties, etc.) is defined in the same way as described above for the meshed structures from SSGM.

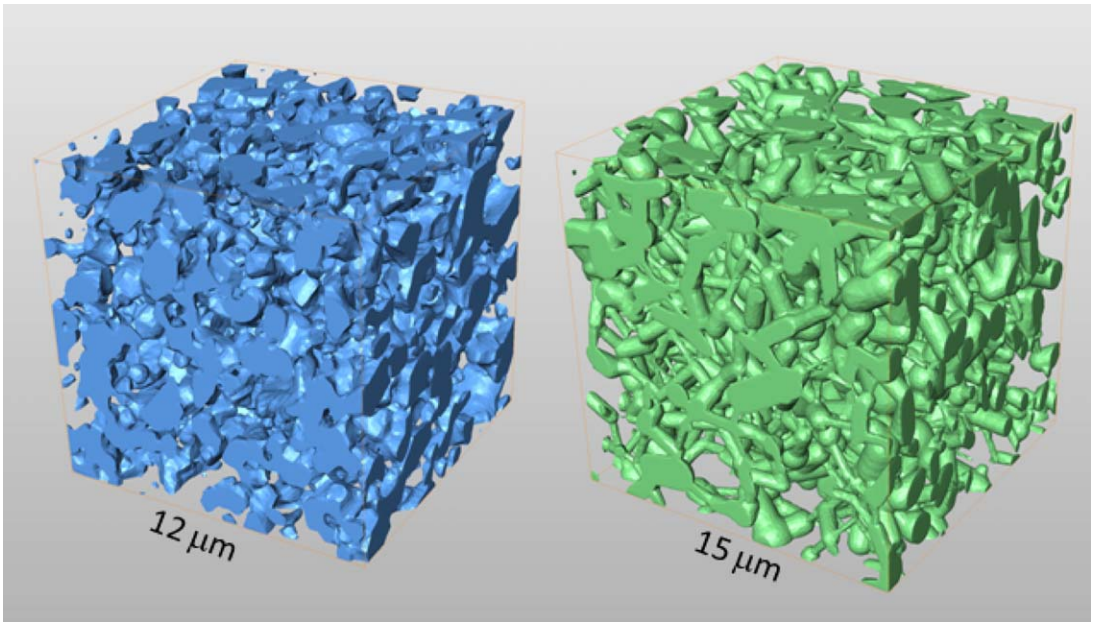

Figure 9. Visualization of meshed grids for FE simulation.

Left: nickel phase in SOFC anode before redox, based on FIB-tomography; right: grid representation of a virtual structure generated with SSGM, which has the same morphological characteristics (i.e., same ε, τ, β) as the nickel phase in the anode before redox. [Color figure can be viewed in the online issue, which is available at wileyonlinelibrary.com.]

Results

In this section, we present the results obtained by our VMT approach. First, we document the range of virtual microstructures that were realized with both, the SSGM and the HBM. The virtual 3-D microstructures are used as structural input for FE simulations. As a result, the corresponding effective transport properties (i.e., the *M*-factors) are obtained. To validate our VMT approach, we compare our results from virtual structures to those from two real SOFC anodes.

Synthetic 3-D microstructures

Figure 10 illustrates the range of structural parameters, which is covered by the microstructures used in this study. We distinguish between two classes of microstructures: 3-D microstructures gained from the SSGM are shown in black and microstructures drawn from the HBM are shown in green. We have performed a large simulation study with SSGM, where the parameter space of the stochastic model is systematically scanned, that is, we simulate a 3-D microstructure for each parameter constellation of the set

$$\{(\lambda,\alpha,g_1,g_2):\lambda\in\{1000,2000,\ldots,6000\},\alpha\in\{0.5,1,\ldots,5\}$$
$$g_1\in\{2,3,\ldots,12\},g_2\in\{2,3,\ldots,12\}\}$$

In this way, we generate 7260 microstructures where each of them is given by a 3-D image stack of size 500×500×500 with cubic voxels. The size of the image window exceeds the representative elementary volume, that is, the variation of the structural characteristics computed on

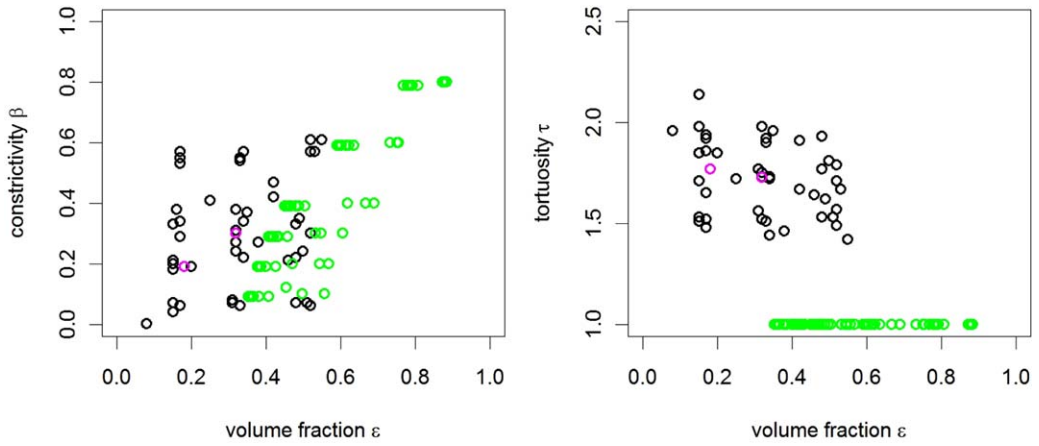

Figure 10. Illustration of parameter constellations obtained from the 107 microstructures, which are selected for transport simulation by FEM.

The two plots show the variation of constrictivity (left) and geometric tortuosity (right) as a function of volume fraction (*x* axis). Black = structures from SSGM, green = HBM, pink = FIB-tomography of Ni-YSZ anodes. [Color figure can be viewed in the online issue, which is available at wileyonlinelibrary.com.]

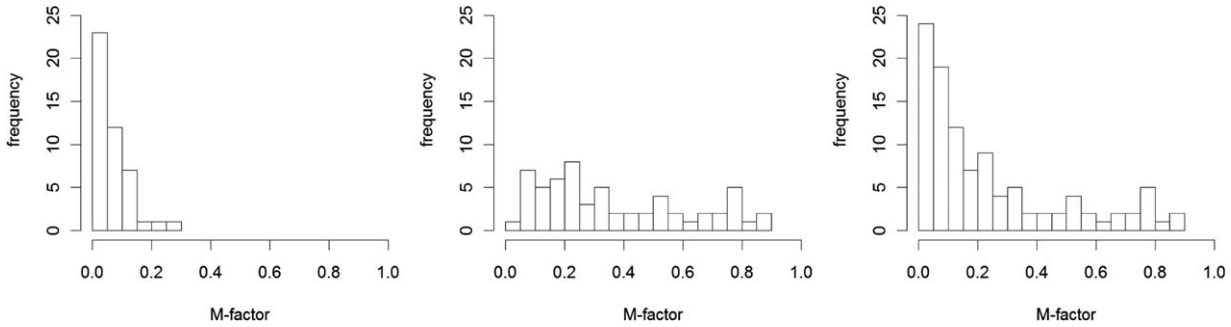

Figure 11. Histograms of the *M*-factors computed by FE simulations for the microstructures drawn from the SSGM (left), from the HBM (center), and from the SSGM and HBM (right).

replications for a fixed parameter constellation is small. For all these simulated microstructures, the structural characteristics ε, τ, and β are computed. For the subsequent FE simulations, the voxel-based realizations of virtual microstructures have to be transformed into structural grids (i.e., meshes). Thereby, two sets of SSGM structures are chosen. One set consists of 36 "realistic microstructures," which means that they cover a similar range of structural parameters as we typically observe in our experimental studies of SOFC electrodes (see e.g., Ref. 6)

$$\{(\varepsilon,\beta,\tau) : \varepsilon \in \{0.15, 0.325, 0.5\}, \beta \in \{0.05, 0.2, 0.28, 0.55\}, \tau \in \{1.5, 1.85, 2.0\}\}$$

To obtain microstructures with these characteristics, the database with 7260 structural 3-D scenarios from SSGM is scanned for parameter constellations that are closest to the predefined characteristics. Thereby, we also selected two structural scenarios, which have equivalent parameters as the nickel phase in the two SOFC anodes used for experimental validation. In a second set, we select nine structures with rather "extreme constellations" of the structural characteristics to extend the statistical basis and to obtain a more generalized picture of the micro–macro relationship, as follows

$$(\varepsilon,\beta,\tau) \in \{(0.002, 0.08, 1.96), (0.16, 0.38, 3.93), (0.86, 0.68, 1.55), \ldots\}$$

It has to be emphasized that the parameters in the SSGM structure are not fully independent from each other. However, for extreme constellations of constrictivity, we can use the HBM.

Experimental and numerical investigations[7,37] indicate that the geometric tortuosity in isotropic materials varies only in a limited range. In particular, these studies indicate that variations of effective transport properties are not primarily induced by tortuosity, as it is often reported, for example, in experimental studies. Instead, in many cases the bottleneck effect may play a more important role for the transport properties. To test this hypothesis, we generate simplified microstructures of straight tubes (geometric tortuosity = 1) with varying cross-sections, by using the HBM. In Figure 10, the HBM structures are indicated with green symbols. The goal of the simulation study based on the HBM is to produce a bunch of microstructures with a large spectrum (in particular, including extreme values) of ε and β. For this purpose, the parameters (r_1, r_2, d_m) of the model are varied, where we produce tubes with deterministic bottlenecks (Figure 7, center) by putting $r_1 = r_2$ and random bottlenecks $r_1 < r_2$ (Figure 7, right). For generating the "deterministic" structures, the parameters of the HBM are varied with respect to the set $\{(r_1, r_2, d_m) : r_1 = r_2, r_1 \in \{10, 20, 30, 40, 60, 80\}, d_m \in \{0.01, 0.1, 0.25, 0.5, 1, 2, 4\}\}$ and for the "random" structures with respect to the set $\{(r_1, 100, d_m) : r_1 \in \{10, 20, 30, 40, 60, 80\}, d_m \in \{0.1, 0.5, 2\}\}$.

In total, we have created 105 virtual 3-D microstructures, as illustrated in Figure 10. Note that 45 structures are drawn from the SSGM (Figure 10, black symbols). Sixty structures are simulated by means of the HBM (Figure 10, green). In addition, from two FIB-SEM analyses of cermet anodes, we have extracted the 3-D structures of the corresponding Ni-phases, (Figure 10, pink).

FEM results

Effective electrical conductivities are computed by means of FE simulations for all of the 105 virtual microstructures. Thereby, we assume an arbitrary value for the intrinsic conductivity of 1 S/cm. In this way, the effective electrical conductivity is identical with the *M*-factor, which describes the sum of all microstructure effects [see (4)]. Figure 11 shows histograms of the resulting effective conductivities and *M*-factors, respectively. We see that the values for microstructures drawn from the SSGM are located in the interval [0.0, 0.3], whereas the values based on the HBM are uniformly spread in the interval [0.0, 1.0]. Thus, the range of effective conductivities computed for the data generated by the SSGM corresponds with the *M*-factors measured for "realistic" functional materials as, for example, SOFC anodes (compare with results in Ref. 6). In contrast, the *M*-factors based on the HBM span over a wider range and they also include extremely high values up to 0.9, where the microstructure effect on transport is almost negligible. Combining both datasets, we cover a large range of *M*-factors with the corresponding microstructures.

In the next section, we use the database consisting of microstructural characteristics ε, τ, β, and computed M_{sim} via FEM for the 105 virtual microstructures in order to investigate the relationship between microstructural features and corresponding effective transport properties in detail.

Discussion

The first goal of this section is to check the accuracy of the hitherto existing formulas for predicting the influence of microstructure on effective transport properties (i.e., prediction of *M*-factors). Therefore, we substitute the computed structural characteristics (i.e., ε, τ, and β) from virtually generated microstructures described in the previous section into formulas (5)–(7). The resulting predictions are subsequently

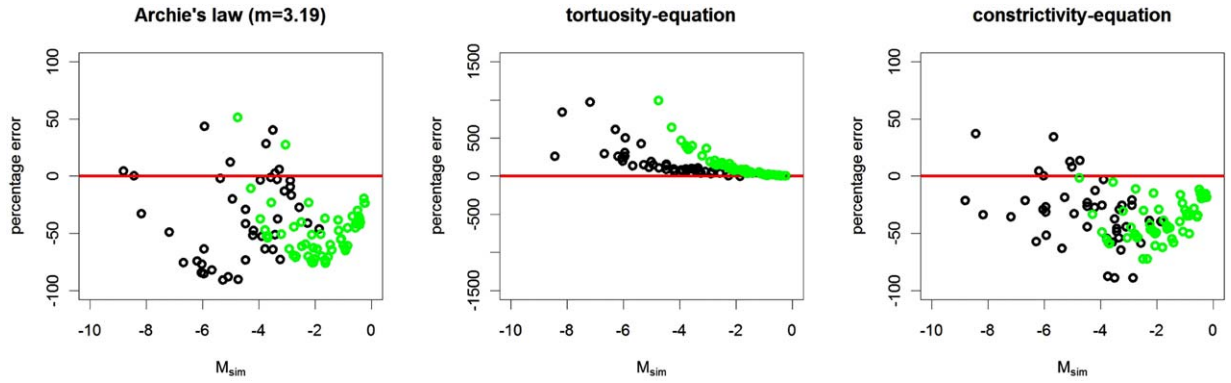

Figure 12. Percentage errors calculated from the difference between simulated (via FEM) and predicted *M*-factors, whereby the predictions are based on one of the known formulas (5), left, (6), middle, and (7), right.

The errors of 105 virtual microstructures are plotted against the simulated *M*-factors on the $\log_2$ scale. Data based on the SSGM and HBM are plotted in black and in green colors, respectively. [Color figure can be viewed in the online issue, which is available at wileyonlinelibrary.com.]

called "M_{pred}." These values are then compared with the *M*-factors obtained from FE simulations, which are performed on meshed grids representing the virtual microstructures. The results from FE simulations are subsequently termed "M_{sim}." It turns out that the predictive capabilities of the three formulas do not lead to satisfying results (i.e., significant differences occur between M_{pred} and M_{sim}). Thus, in a second step, we introduce modifications of the known formulas. With these modifications, the predictive capability can be improved significantly.

Predictive capability of formulas from literature

For the evaluation of the predictive capabilities, we introduce a quality criterion, which is the mean absolute percentage error (MAPE) of predicted and simulated *M*-factors. More precisely, let $(x_1,\ldots,x_n)$ be the predicted values obtained by substitution of ε,τ, and β in one of the three known formulas and let $(y_1,\ldots,y_n)$ be the corresponding simulated values from FEM. Then, the MAPE of $(x_1,\ldots,x_n)$ and $(y_1,\ldots,y_n)$ is given by

$$\text{MAPE}\left((x_1,\ldots,x_n),(y_1,\ldots,y_n)\right)=\frac{1}{n}\sum_{i=1}^{n}\frac{|x_i-y_i|}{y_i}100$$

The MAPE values are determined in two different ways: $\text{MAPE}_{\text{total}}$ is based on all 105 virtual microstructures, and $\text{MAPE}_{\text{SSGM}}$ includes only 45 structures from SSGM. The latter selection is motivated by the fact that the morphological characteristics in microstructures drawn from the SSGM are much closer to those in real microstructures (as observed in our experimental investigations of SOFC electrodes[5,6,22]). In contrast, the microstructures drawn from the HBM extend the range of structural characteristics to high *M*-values, which, however, may not be relevant for most practical applications. Because this evaluation is focusing mainly on the prediction of realistic microstructures, the $\text{MAPE}_{\text{SSGM}}$ is considered as being more relevant for practical applications than the $\text{MAPE}_{\text{total}}$. The MAPE is determined separately for each of the three formulas (5), (6) and (7) from literature. To apply Archie's law, it is necessary to determine the exponential factor *m*, compare Eq. 5. For reasons stated above, Archie's *m*-exponent is fitted to the data based on the SSGM, that is, *m* is chosen such that the $\text{MAPE}_{\text{SSGM}}$ is minimized. This optimization problem is solved by the simulated annealing algorithm[41] being a stochastic optimization technique, which can handle global optimization problems. As a result, we obtain $m=3.194$ for the exponent of ε in Archie's law. Figure 12 shows the percentage errors of predicted and simulated *M*-factors for each of the 105 microstructures that were generated with SSGM (black) and with HBM (green). Note that in the ideal case of a perfect prediction the percentage errors of each data point would be located on the horizontal line $\{(x,y)\in\mathbb{R}^2 : x=0, y=0\}$ (red line of Figure 12). Hence, a small mean percentage error (MAPE) is taken as an indication for good predictions. The percentage errors ($\text{MAPE}_{\text{SSGM}}$ and $\text{MAPE}_{\text{total}}$) for the three formulas (5), (6), and (7) are summarized in Table 1. The results indicate that predictions based on Archie's law (5) (with $m=3.194$) and on the constrictivity equation (7) have a much better quality (with $\text{MAPE}_{\text{SSGM}}\leq 50$) than predictions based on the tortuosity equation (6) (with $\text{MAPE}_{\text{SSGM}}=341$). On a first glance, the relatively small errors obtained with Archie's law are surprising, considering the fact that it only takes into account the phase volume fraction ε and it neglects information of tortuous pathways and narrow bottlenecks in terms of τ and β, respectively. However, it must be noticed, that the application of Archie's law requires a preceding fit of the *m*-factor (as explained earlier). Hence, the percentage error for Archie's law can be expected to be relatively small, because its prediction includes a fitting procedure. In contrast, the predictions with the tortuosity and constrictivity equations (6) and (7) do not include any preceding fitting and they are, therefore, considered as being more "honest" predictions. Nevertheless, the percentage errors for the tortuosity equation in Figure 12 are relatively high. Furthermore, a trend can be observed with increasing errors for decreasing *M*-factors. Hence, the stronger the microstructure effect, the more the tortuosity equation overestimates the effective transport properties. This trend

Table 1. $\text{MAPE}_{\text{SSGM}}$ and $\text{MAPE}_{\text{total}}$ Computed for M_{pred} and M_{sim} where M_{pred} is Based on the Three Known Formulas (5), (6), and (7)

	Archie's Law (5)	Tortuosity equation 6	Constrictivity equation 7
$\text{MAPE}_{\text{SSGM}}$	47	341	37
$\text{MAPE}_{\text{total}}$	50	625	37

Table 2. Fitted Parameters of the Formulas (8)–(14) by Means of the Simulated Annealing Algorithm

Equation Matrix	a	b	c	d	$\mathrm{MAPE}_{\mathrm{SSGM}}$	$\mathrm{MAPE}_{\mathrm{total}}$
8	2.346	1.569	0.709	2.298	15	25
9	–	1.327	0.689	1.478	25	28
10	1.105	3.27	–	–	46	48
11	2.943	3.136	–	2.01	45	47
12	1.04	2.194	0.58	–	34	44
13	2.03	1.57	0.724	2 (fixed)	16	20
14	–	1.156	0.668	2 (fixed)	27	26

indicates that the small M-factors are not well explained when only the tortuosity effect is taken into account. A better prediction is obtained with the constrictivity equation, which has relatively small percentage errors also for data points with small M-factors. Obviously, the bottleneck effect represents an important morphological feature that needs to be included for predictions of the effective transport properties, especially in samples with a strong microstructure effect.

Predictive capability of modified formulas

In this section, we modify the formulas (5)–(7) to improve the quality of prediction of the M-factor and to decrease the percentage errors. In particular, we are interested in parametric classes of functions

$$f : [0,1]\times[0,1]\times[1,\infty] \rightarrow [0,1]; \quad (\varepsilon,\beta,\tau)\mapsto f(\varepsilon,\beta,\tau)$$

where $f(\varepsilon,\beta,\tau)$ predicts the microstructure influence (i.e., M-factor) on the effective transport properties.

Parametric Classes of Functions. As a first modification approach, we consider a parametric class of functions f, which can be seen as a generalization of the constrictivity equation (7), that is

$$f(\varepsilon,\beta,\tau)=\min\left\{\frac{a\varepsilon^b\beta^c}{\tau^d},1\right\}\in[0,1] \text{ with } a,b,c,d\in\mathbb{R} \quad (8)$$

Thus, for the generalization of Eq. 7 we have introduced additional degrees of freedom, in particular, by a linear prefactor a and exponential parameters b,c, and d, which describe the varying impact of ε,τ, and β on transport. In the following, we introduce simplified versions of this modified formula. By comparison with the simulated M-factors, we then optimize the parameters a,b,c, and d to achieve a small $\mathrm{MAPE}_{\mathrm{SSGM}}$, which is used as a quality indicator. A good quality of the fit indicates that a specific function of ε,τ, and β potentially captures the relevant features of the microstructural effects.

We introduce modifications that help to understand whether or not the prefactor a of (8) is of importance. For this purpose, we compare Eq. 8 with the following class, where the prefactor is put to $a=1$

$$f(\varepsilon,\beta,\tau)=\frac{\varepsilon^b\beta^c}{\tau^d}\in[0,1] \text{ with } b,c,d\in\mathbb{R} \quad (9)$$

In addition, we study the influence of the constrictivity factor β and the geometric tortuosity τ on the effective transport properties. For this purpose, we consider the following three classes

$$f(\varepsilon)=\min\left\{a\varepsilon^b,1\right\}\in[0,1] \text{ with } a,b\in\mathbb{R} \quad (10)$$

$$f(\varepsilon,\tau)=\min\left\{\frac{a\varepsilon^b}{\tau^d},1\right\}\in[0,1] \text{ with } a,b,d\in\mathbb{R} \quad (11)$$

$$f(\varepsilon,\beta)=\min\left\{a\varepsilon^b\beta^c,1\right\}\in[0,1] \text{ with } a,b,c\in\mathbb{R} \quad (12)$$

Moreover, we are also interested in the influence of the tortuosity-exponent d. In literature, it is widely accepted that the impact of tortuosity on the transport is described by τ^{-2} see Ref. 22. For comparison, we thus introduce expressions where the exponent d of τ in (8) and (9) is fixed to 2. This class is investigated once with a prefactor a and once without a prefactor. Consider

$$f(\varepsilon,\beta,\tau)=\min\left\{\frac{a\varepsilon^b\beta^c}{\tau^2},1\right\}\in[0,1] \text{ with } a,b,c\in\mathbb{R} \quad (13)$$

$$f(\varepsilon,\beta,\tau)=\frac{\varepsilon^b\beta^c}{\tau^2}\in[0,1] \text{ with } b,c\in\mathbb{R} \quad (14)$$

Choice of Parameters. In the next step, the parameters for each class of functions are chosen such that the corresponding $\mathrm{MAPE}_{\mathrm{SSGM}}$ is minimized. This optimization problem is solved again by means of the simulated annealing algorithm. The fitted parameters of the formulas (8)–(14) and the corresponding MAPEs are listed in Table 2. Based on the fitted parameters from SSGM, we then also evaluate the $\mathrm{MAPE}_{\mathrm{total}}$, which considers all 105 virtual microstructures. It basically indicates whether the expression fitted for realistic microstructures (SSGM) is also capable to predict the micro–macro relationships in samples with high M-factors (represented by structures from HBM).

In Figure 13, percentage errors resulting from the difference between predicted and simulated M-factors are plotted against M_{sim} from FEM for each of the modified formulas. For the discussion of these results, we first consider the basic form of the equations (i.e., whether or not it includes constrictivity or tortuosity) and the corresponding impact on the quality of prediction, represented by $\mathrm{MAPE}_{\mathrm{SSGM}}$. In a second step, we then discuss details in the modifications of the favored type of equation.

Equation 10 has a simple form, which only takes into account ε. It can be considered as a modification of Archie's law. Its $\mathrm{MAPE}_{\mathrm{SSGM}}=46$, which is nearly identical to the one obtained with the conventional form of Archie's law $\mathrm{MAPE}_{\mathrm{SSGM}}=47$. Equation 11 represents a modification of the tortuosity equation. The corresponding $\mathrm{MAPE}_{\mathrm{SSGM}}$ is 45, which is a significant improvement compared to the conventional tortuosity equation with a $\mathrm{MAPE}_{\mathrm{SSGM}}$ of 341. But, it is still relatively high. Hence, the two equations, which do not include β, have a poor predictive capability. Equation 12, which includes β but excludes τ has a $\mathrm{MAPE}_{\mathrm{SSGM}}$ of 34, which is only a moderate improvement. In contrast all equations, which include all three parameters ε,τ, and β, have significantly lower $\mathrm{MAPE}_{\mathrm{SSGM}}$ between 15 and 27. These equations [i.e., (8), (9), (13), and (14)] represent modifications of the constrictivity equation. The most general expression of this type is given by (8). Hence, modifications

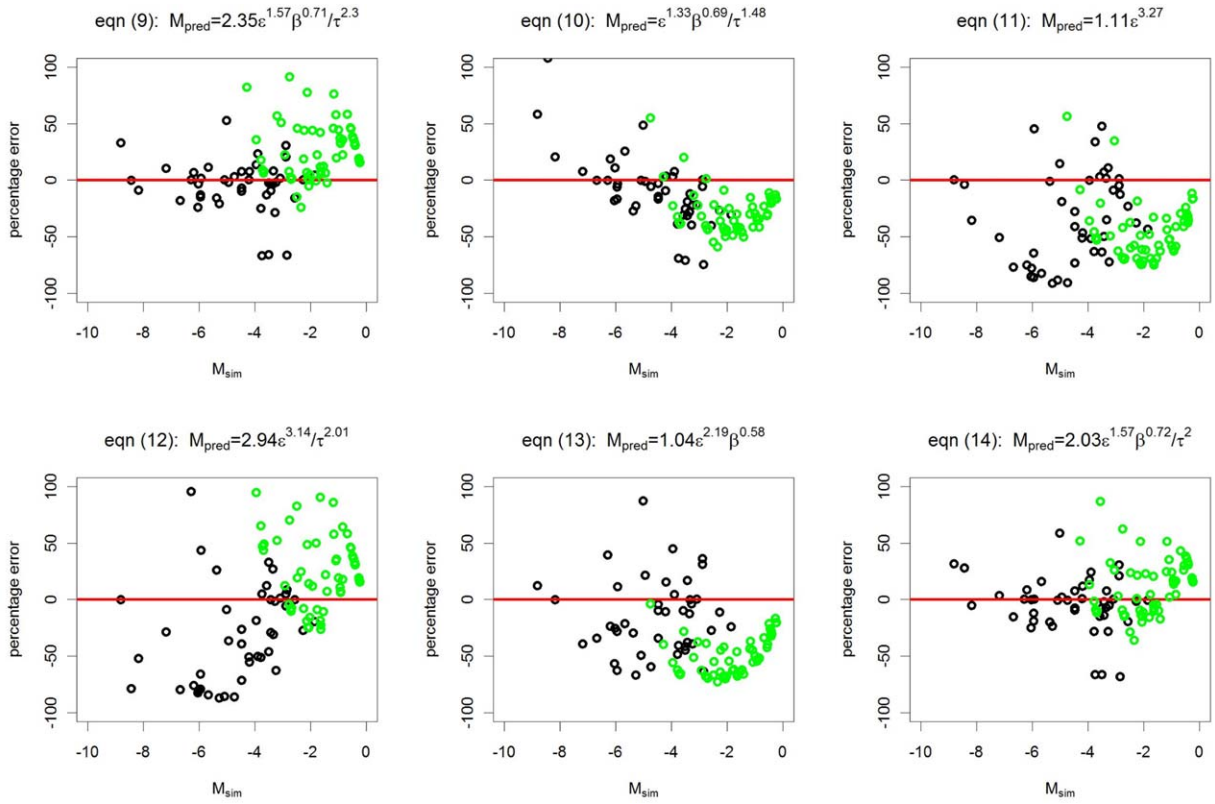

Figure 13. Percentage errors originating from the difference between M_{sim} (via FEM) and M_{pred} using formulas (8)–(14) plotted against M_{sim} given on the $\log_2$ scale.

Data based on the SSGM (HBM) are plotted in black (green) color. [Color figure can be viewed in the online issue, which is available at wileyonlinelibrary.com.]

of the constrictivity equation are considered as the most suitable type of expression, which provide a precise prediction of the transport properties. In the following section, we discuss different modifications of this type of expression.

Influence of Particular Parameters. ***Influence of Prefactor a.*** Comparable modifications with and without prefactor a tend to have the better fits (smaller $\mathrm{MAPE}_{\mathrm{SSGM}}$) when a prefactor is used (cf. e.g., Eqs. 8 vs. 9, 13 vs. 14). The fit with the general Eq. 8 results in a prefactor of 2.34. When the tortuosity exponent d is fixed to $d=2$ in (13), then the prefactor is close to 2.0. Thus, based on the virtual testing, a prefactor a of $a \in [2.0, 2.34]$ seems to be necessary. In this context, it must be emphasized that the structural parameters such as β and τ in complex disordered materials have no simple geometric definition. Instead, the measurement of these parameters depends on specific geometric concepts for image analysis (such as "shortest pathways" and "median axis"). Therefore, it seems justified to introduce an empirically derived prefactor, which describes the relationship between the measured geometric parameters with the M-factor and with the corresponding effective transport properties.

Influence of Exponent b of Volume Fraction ε**.** To obtain adequate weighting of volume fraction, which effectively contributes to the transport, ε must be corrected by the bottleneck effect. This can be achieved by multiplying the total volume fraction ε with constrictivity β. In all equations, which include constrictivity, the exponent b is usually below 2. For the expressions with the lowest $\mathrm{MAPE}_{\mathrm{SSGM}}$, that is, for the generalized form (8) and its equivalent with a fixed tortuosity of 2.0, that is, (13), b becomes 1.57. In those cases, where constrictivity β is not included [c.f. (10), (11)], relatively large values of b are necessary to capture the apparent influence of volume fraction ε. This is a further argument, which documents the importance of the

Table 3. Compilation of Structural Characteristics $(\varepsilon, \beta, \tau)$ and Different M-Factors from Simulation (M_{sim}), from Prediction with Eq. 13 (M_{pred}), and from Conductivity Measurement (M_{meas}) for Ni-Cermet Anodes and SSGM Data

	Method	Sample	Color (Figure 14)	ε	β	τ	M_{sim} (1a–2b) M_{meas} (3a,3b)	M_{pred}	$M_{sim}-M_{pred}$	%-Error
1a	FIB-SEM	Anode before redox	Blue	0.32	0.3	1.73	0.077	0.048	0.029	60.4
1b	FIB-SEM	Anode after redox	Blue	0.18	0.19	1.78	0.006	0.013	−0.007	−53.8
2a	SSGM	Fitted to 1a	Gray	0.32	0.31	1.73	0.045	0.049	−0.004	−8.2
2b	SSGM	Fitted to 1b	Gray	0.19	0.19	1.85	0.016	0.013	0.003	23.1
3a	Four-point measurements	Anode before redox	Pink	0.32	0.3	1.73	0.027	0.048	−0.021	−43.8
3b	Four-point measurements	Anode after redox	Pink	0.18	0.19	1.78	0.01	0.013	−0.003	−23.1

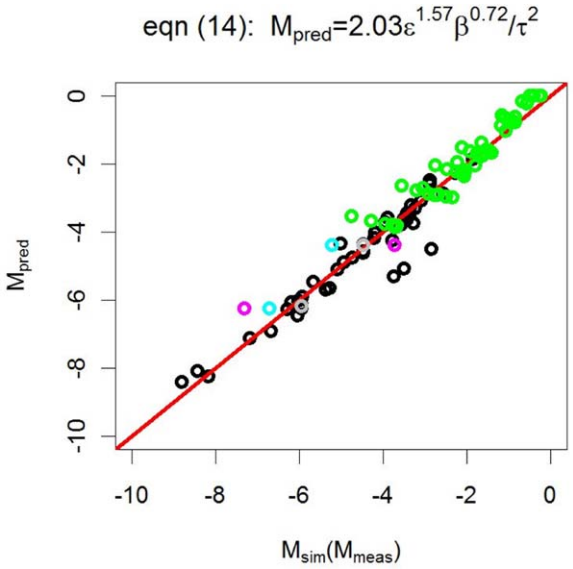

Figure 14. Comparison of *M*-factors simulated by FEM M_{sim} and predicted by formula (13) M_{pred} for microstructures generated by SSGM (black), HBM (green), experimental 3-D anode data sets (blue, or pink when referring to M_{meas} instead of M_{sim}), and corresponding SSGM microstructures fitted to the experimental microstructures (gray).

M_{sim} (M_{meas}) given on the $\log_2$ scale plotted against M_{pred}. [Color figure can be viewed in the online issue, which is available at wileyonlinelibrary.com.]

constrictivity parameter for the prediction of effective transport properties.

***Influence of* Exponent c *of* Constrictivity β.** For the exponent c of constrictivity β, all results of the fitting give c-values in a relatively narrow range around 0.6–0.7. For the favored Eqs. 8 and 13, c is 0.71 and 0.72. The exponential behavior indicates that for microstructures with very narrow bottlenecks (i.e., $\beta < 0.1$) a small change of the neck dimensions has a large impact on the effective transport properties. In contrast, when constrictivity is close to 1 (i.e., "open" cylindrical pores), then the transport properties are less sensitive to variations of β.

***Influence of* Exponent *d of* Tortuosity τ.** Based on theoretical considerations it is concluded that the exponent d of tortuosity should be 2.0 (as discussed earlier, see also Ref. 13). The fit of the generalized Eq. 8 results in a d-value of $d=2.3$ with a relatively small mean percentage error ($MAPE_{SSGM}=0.15$). A similarly small $MAPE_{SSGM}$ of 0.16 is obtained when d is fixed to $d=2.0$ [see (13)]. Hence, these results and the theory consistently point to a value of (approximately) 2.0 for the exponent d of tortuosity.

In summary, the modified formulas (8) and (13) lead to very good predictions of *M*-factors, which have significantly lower $MAPE_{SSGM}$ than the three formulas from literature. Thereby, the Eq. 13 is preferred by the authors due to its simplicity. This equation represents a modification of the constrictivity equation, whereby the exponent of tortuosity is fixed to $d=2.0$, which is in accordance with theoretical considerations in literature. The exponential behavior of $\beta^{0.72}$ documents a strong influence of constrictivity on the transport properties, in particular for structures with low *M*-factors. Furthermore, this expression exhibits the lowest $MAPE_{total}$, which indicates that it is capable to capture the relevant microstructure effects over the entire range of *M*-factors, including the HBM-structures.

Validation of VMT approach

To validate the VMT approach, we compare the results with experimental data of a Ni-YSZ anode for SOFC. The electric conductivity was determined by a four-point measurement under anode conditions for the original anode (before) and for an anode that was exposed to eight redox-cycles (as described in Ref. 6). The results are summarized in Table 3. We obtain three pairs of samples, which represent the anode microstructures before and after redox cycling: (1a/1b) real microstructures from FIB-tomography, (2a/2b) virtual microstructures from SSGM, which have identical structural characteristics as the real ones from FIB-tomography, and (3a/3b) real samples, which are used for conductivity measurements. In a first step, we consider the change of *M*-factors due to the redox degradation. The experimental measurements show that the effective electrical conductivity is 2.7% of the intrinsic conductivity (i.e., M_{meas} of $3a=0.027$). On redox cycling this value drops to 1% (i.e., M_{meas} of $3b=0.01$). This drop of conductivity can be attributed to changes of constrictivity (β) and volume fraction of connected Ni-phase (ε), whereas the geometric tortuosity (τ) is almost unaffected by the Nickel degradation. FE-simulations based on structural input from FIB-tomography (of Ni-phase in the real SOFC anodes) also show a significant drop of M_{sim} from 7.7% (1a) to 0.6%/(1b). Furthermore, also the FE-simulations based on virtual structures from SSGM (with identical structural characteristics as (1a/1b) show a significant drop from 4.5% (2a) to 1.6% (2b). Hence, all three pairs show the same trend in the influence of redox degradation, which leads to a drop of *M*-factors and associated effective electrical conductivities. Using Eq. 13 with the fitted values for prefactor and exponents as given in Table 3, we can predict the effective conductivities (i.e., M_{pred}) based on ε, τ, and β. Because all three pairs have (almost) identical structural characteristics, these predictions result in (almost) identical values for M_{pred} of (4.8) 4.9% before and 1.3% after redox cycling. As shown in Table 3, the simulations based on virtual microstructures from SSGM perfectly match with the predictions (i.e., difference of <0.3%). However, for the real microstructures the simulated (M_{sim}; 1a, 1b) and the measured values (M_{meas}; 3a, 3b) differ up to 2.9%, which corresponds to a %-error [i.e., $(M_{sim}-M_{pred})/M_{pred}$] of 60.4 (see 1a). Because the *M*-factors are quite low, a difference of a few % results in rather large %-errors for some of the data-points. The reason for the relatively large %-errors can be multifold. Each set of data bears some uncertainties (e.g., contacting problem in experimental conductivity measurements, segmentation uncertainty in image analysis of FIB-tomography). In addition, one also has to take into account that there are potential differences between the virtual microstructures from SSGM and the real microstructures from FIB-tomography, which are currently not captured with ε, τ, and β. This scenario is, for example, likely to occur when the real microstructures contain so-called "dead ends." For an accurate prediction of such effects an additional structural parameter needs to be introduced. In summary, a comparison of virtual with experimental data indicates, that predictions based on Eq. 13 and with structural parameters (ε, τ, β) are

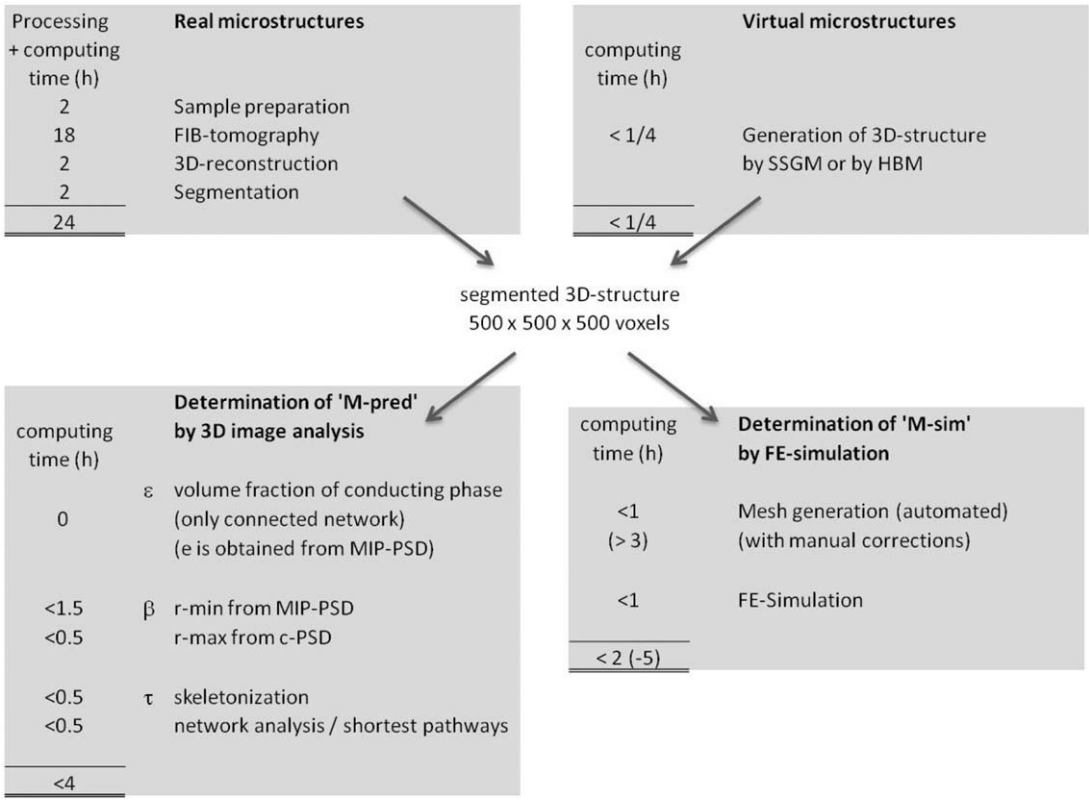

Figure 15. Overview of processing steps for the study of microstructure influences on effective transport properties.

The computation time may vary with the type of microstructure under consideration. It should also be noted, that for some steps the manual set-up of the procedure requires considerable amount of time, which is included in the estimated "computing time."

capable to capture the effective electrical conductivity with a precision of a few percentages. This is sufficient to predict, for example, the trends of redox degradation in SOFC anodes. However, the %-errors for structures with low M-factors are relatively large. At this stage, the source of the %-errors cannot be determined conclusively.

Comparison of different approaches for the study of microstructure effects

In this study, we use different approaches to describe the influence of microstructures on the effective transport properties. Figure 15 summarizes the corresponding computing (and processing) times of each step in the workflow. We consider 3-D structures consisting of 500^3 voxels. When analyzing real samples the total acquisition time by FIB-tomography and subsequent 3-D reconstruction is approximately 24 h. In contrast, virtual microstructures can be generated, for example, with SSGM in less than 15 min. Hence, for a parametric study with numerous different samples the VMT approach is much more efficient, whereas the experimental approach with real microstructures may be too slow (and also too expensive). Nevertheless, real experimental data is required for the validation of the VMT approach. The influence of the microstructure on effective transport properties can then be described either via image analysis (i.e., with M_{pred}) or by FE-simulation (i.e., with M_{sim}). For M_{pred}, the determination of ε, τ, β requires approximately 0.5–4 h, whereas M_{sim} can be obtained by FE-simulation (including mesh generation) in approximately 2–5 h (also depending how much manual adjustments are necessary). Hence, the approach with FE-simulation is comparably fast. However, it must be emphasized that image analysis provides detailed insight into microstructure effects, which cannot be achieved by FE-simulation. For example, the performance degradation of an SOFC anode (i.e., drop of electrical conductivity, as discussed earlier), can be assigned to the decrease of connectivity in the network of the nickel phase (ε) and to a drop of constrictivity (β), based on results from 3-D image analysis. This example illustrates, that the recent progress in image analysis, which allows quantitative description of critical microstructure parameters, together with the quantitative relationships (as presented in this study) represents a powerful combination of methods, which opens new possibilities for the study of microstructure effects. This is important not only for the study of degradation mechanisms but it can also be useful for improved materials processing due to knowledge based microstructure optimization.

Conclusions

In this article, we investigate the hypothesis that effective transport properties such as electric conductivity in a porous SOFC electrode can be predicted based on the critical structural parameters (i.e., ε, τ, β). In literature, the link between effective transport properties and microstructure parameters is described with different expressions for the M-factor. Here, we investigate the predictive capabilities of Archie's law (5), tortuosity equation (6), and constrictivity equation (7). For this purpose, we use a VMT approach based on stochastic simulation. VMT enables to build up an extensive database consisting of 105 microstructures characterized in

terms of the relevant volume-averaged characteristics ε, τ, and β by 3-D image analysis and their corresponding M-factors gained by FE simulations. The quality of prediction is characterized by the so-called MAPE, which considers the difference between predicted and simulated M-factors for the entire set of chosen microstructures. It turns out that predictions based on Archie's law [(5) depending solely on ε] and on the well-known tortuosity equation [(6), which is a function of ε and τ] have limited or even a poor qualities. Better results are achieved with the constrictivity equation (7), which is a function of all three structural parameters $(\varepsilon, \tau, \beta)$. The quality of prediction can be further improved by introducing modifications of the constrictivity equation, which include a linear prefactor and exponential coefficients for ε, τ, and β. The prefactor and the coefficients are determined with a fitting procedure, which minimizes the MAPE of the modified expressions. Based on these methodologies and by taking into account, the large database from VMT the following equation [cf. (13)] can be postulated as an empirical expression with a high predictive capability for the M-factor and associated effective transport properties

$$M = 2.03\varepsilon^{1.57}\beta^{0.72}/\tau^2$$

With this expression, a good quality of prediction is achieved as well for microstructures that are similar to the ones in real technical materials such of SOFC electrodes (i.e., $\mathrm{MAPE}_{\mathrm{SSGM}} = 16$), as also for HBM structures with extreme configurations such as high volume fractions or high constrictivities (i.e., $\mathrm{MAPE}_{\mathrm{total}} = 20$). Based on the results from all modified expressions (8)–(14), a strong correlation is identified between volume fractions and M-factors. Hence, as a first approximation, the effective transport properties are dominated by ε. However, the results also document that constrictivity has an essential influence on the M-factor. This influence of β is particularly strong for materials with low M-factors (i.e., with a strong bottleneck effect). Finally, also the influence of geometric tortuosity is significant due to the corresponding exponent of 2. The VMT approach is validated by comparison with experimental results from two SOFC anodes before and after redox degradation. It is shown that the favored expression (13) is capable to predict qualitatively the influence of microstructure degradation on effective electrical conductivity. Apparently, for microstructures with a low M-value, the %-error [i.e., the relative difference between M_{pred} and M_{sim} (or M_{meas})] are quite large (up to 60%) and the reasons for this uncertainty are not yet identified conclusively. Hence, more experimental work needs to be done for the validation of the VMT approach. In summary, the investigations based on the VMT approach give deeper insight into the relationship between microstructure and effective transport properties. It must be emphasized that the study is only valid for composite microstructures where transport takes place in a single phase. In future, the postulated relationship (13) can be used to describe the influence of microstructure on electric or ionic conductivity in composite materials. This is of particular interest for studies dealing with materials for energy conversion such as electrodes of fuel cells and batteries or membranes in electrolysis cells.

Acknowledgments

The authors thank the following persons for contributing with very valuable input: Beat Münch and Lukas Keller (image analysis), Guido Sartoris (finite element modelling), Boris Iwanschitz (SOFC experiments), and Philippe Gasser (FIB-tomography). The research presented in this article has received funding from various sources. L. Holzer was supported by the European Union's Seventh Framework Program (FP7/2007–2013) for the Fuel Cells and Hydrogen Joint Undertaking under grant agreement No. 256885 (project "SOFC-life") and by the Swiss national project "SOF-CH" (SFOE/BFE project No. SI 500'084). O. Pecho was supported by SNF (Swiss National Science Foundation, Grant No. 200021_135270). All financial supports are gratefully acknowledged.

Literature Cited

1. Bird RB, Stewart WE, Lightfoot EN. *Transport Phenomena*. New York: Wiley, 2007.
2. Keller LM, Holzer L, Schuetz P, Gasser P. Pore-space relevant for gas permeability in opalinus clay: statistical analysis of homogeneity, percolation and representative volume element (RVE). *J Geophys Res*. 2013;118:1–14.
3. Spanne P, Thovert JF, Jacquin CJ, Lindquist WB, Jones KW, Adler PM. Synchrotron computed microtomography of porous media: topology and transport. *Phys Rev Lett*. 1994;73(14):2001–2004.
4. Berkowitz B, Balberg I. Percolation theory and its application to groundwater hydrology. *Water Resour Res*. 1993;29(4):775–794.
5. Holzer L, Wiedenmann D, Münch B, Keller LM, Prestat M, Gasser P, Robertson I, Grobéty B. The influence of constrictivity on the effective transport properties of porous layers in electrolysis and fuel cells. *J Mater Sci*. 2013;48(7):2934–2952.
6. Holzer L, Iwanschitz B, Hocker T, Keller LM, Prestat M, Pecho O, Sartoris G, Gasser P, Münch B. Redox cycling of Ni-YSZ anodes for solid oxide fuel cells: influence of tortuosity, constriction and percolation factors on the effective transport properties. *J Power Sources*. 2013;242:179–194.
7. Wiedenmann D, Keller LM, Holzer L, Stojadinovic J, Münch B, Suarez L, Fumey B, Hagendorfer H, Brönnimann R, Modregger P, Gorbar M, Vogt UF, Züttel A, Mantia FL, Wepf R, Grobéty B. 3D pore structure and ion conductivity of porous ceramic diaphragms. *Am Inst Chem Eng J*. 2013;59(5):1446–1457.
8. Mahadevan TS, Milosevic M, Kojic M, Hussain F, Kojic N, Serda R, Ferrari M, Ziemys A. Diffusion transport of nanoparticles at nanochannel boundaries. *J Nanopart Res*. 2013;15(3):1477.
9. Archie GE. The electrical resistivity log as an aid in determining some reservoir characteristics. *Trans Am Inst Mining Metallurg Pet Eng*. 1942;146:54–61.
10. Brakel JV, Heertjes PM. Analysis of diffusion in macroporous media in terms of a porosity, a tortuosity and a constrictivity factor. *Int J Heat Mass Transf*. 1974;17:1093–1103.
11. Carman PC. *Flow of Gases through Porous Media*. London: Butterworths, 1956.
12. Kozeny J. Ueber kapillare Leitung des Wassers im Boden. *Sitzungsber Akad Math Naturwiss*. 1927;136a:271–306.
13. Clennell MB. Tortuosity: a guide through the maze. In: Lovell MA, Harvey PK, editors. *Developments in Petrophysics*. London: Geological Society Special Publications, 1997:299–344.
14. Khan F, Enzmann F, Kerten M, Wiegmann A, Steiner K. 3D simulation of the permeability tensor in a soil aggregate on basis of nanotomographic imaging and LBE solver. *J Soils Sediments*. 2012;12(1):86–96.
15. Brinkmann JP, Froning D, Reimer U, Schmidt V, Lehnert W, Stolten D. 3D modeling of one and two component gas flow in fibrous microstructures in fuel cells by using the Lattice-Boltzmann method. *ECS Trans*. 2012;50:207–219.
16. Froning D, Brinkmann J, Reimer U, Schmidt V, Lehnert W, Stolten D. 3D analysis, modeling and simulation of transport processes in compressed fibrous microstructures, using the Lattice Boltzmann method. *Electrochim Acta*. 2013;110:325–334.
17. Cheng X, Sastry AM. On transport in stochastic, heterogeneous fibrous domains. *Mech Mater*. 1999;31(12):765–786.
18. Auer M, Gasser TC. Reconstruction and finite element mesh generation of abdominal aortic aneurysms from computerized tomography angiography data with minimal user interactions. *IEEE Trans Med Imaging*. 2010;29(4):1022–1028.
19. Akolkar A, Petrasch J. Tomography-based characterization and optimization of fluid flow through porous media. *IEEE Trans Med Imaging*. 2012;95(3):535–550.

20. Münch B, Holzer L. Contradicting geometrical concepts in pore size analysis attained with electron microscopy and mercury intrusion. *J Am Ceram Soc*. 2008;91(12):4059–4067.
21. Gaiselmann G, Neumann M, Holzer L, Hocker T, Prestat M, Schmidt V. Stochastic 3D modeling of $La_{0.6}Sr_{0.4}CoO_{3-\delta}$ cathodes based on structural segmentation of FIB-SEM images. *Comput Mater Sci*. 2013;67:48–62.
22. Holzer L, Iwanschitz B, Hocker T, Münch B, Prestat M, Wiedenmann D, Vogt U, Holtappels P, Sfeir J, Mai A, Graulen T. Microstructure degradation of cermet anodes for solid oxide fuel cells: quantification of nickel grain growth in dry and in humid atmospheres. *J Power Sources*. 2011;196(3):1279–1294.
23. Illian J, Penttinen A, Stoyan H, Stoyan D. *Statistical Analysis and Modelling of Spatial Point Patterns*. Chichester: Wiley, 2008.
24. Chiu SN, Stoyan D, Kendall WS, Mecke *J. Stochastic Geometry and its Applications*, 3rd ed. Chichester: Wiley, 2013.
25. Stenzel O, Westhoff D, Manke I, Kasper M, Kroese DP, Schmidt V. Graph-based simulated annealing: a hybrid approach to stochastic modeling of complex microstructures. *Model Simul Mater Sci Eng*. 2013;21:055004.
26. Stenzel O, Hassfeld H, Thiedmann R, Koster LJA, Oosterhout SD, van Bavel SS, Wienk MM, Loos J, Janssen RAJ, Schmidt V. Spatial modelling of the 3D morphology of hybrid polymer-ZnO solar cells, based on electron tomography data. *Ann Appl Stat*. 2011;5:1920–1947.
27. Israelachvili J. *Intermolecular and Surface Forces*. Amsterdam: Academic Press, 1991.
28. Russ JC. *The Image Processing Handbook*. Boca Raton: CRC Press, 1999.
29. Burger W, Burge MJ. *Digital Image Processing—An Algorithmic Approach using Java*. Berlin: Springer, 2007.
30. Jähne B. *Digital Image Processing*, 6th ed. Berlin: Springer, 2005.
31. VSG. *Visualization Sciences Group – Avizo Standard*. Available at http://www.vsg3d.com/avizo/overview. Last accessed date on 2013.
32. Lindquist WB, Lee SM, Coker DA, Jones KW, Spanne P. Medial axis analysis of void structure in three-dimensional tomographic images of porous media. *J Geophys Res*. 1996;101:8297–8310.
33. Bhatia SK. Directional autocorrelation and the diffusional tortuosity of capillary porous media. *J Catal*. 1985;93:192–196.
34. Shen L, Chen Z. Critical review of the impact of tortuosity on diffusion. *Chem Eng Sci*. 2007;62:3748–3755.
35. Katsube TJ, Modford BS, Best ME. Petrophysical characteristics of shales from the Scotian shelf. *Geophysics*. 1991;56:1681–1689.
36. Salem HS, Chilingarian GV. Physical and mathematical aspects of tortuosity in regard of the fluid flow and electric current conduction in porous media: example of the Hibernia and Terra Nova reservoirs, off the eastern coast of Canada. *Energy Sources A*. 2000;22:137–145.
37. Sun Z, Tang X, Cheng G. Numerical simulation for tortuosity in porous media. *Microporous Mesoporous Mater*. 2013;173:37–42.
38. Hirsch C, Neuhäuser D, Schmidt V. Connectivity of random geometric graphs related to minimal spanning forests. *Adv Appl Probab*. 2013;45:20–36.
39. Iwanschitz A, Sfeir J, Mai A, Schütze M. Degradation of SOFC anodes upon redox cycling: a comparison between Ni/YSZ and Ni/CGO. *J Electrochem Soc*. 2010;157(2):B269–B278.
40. .SESES. Available at http://www.zhaw.ch/engineering/icp/software/nm-seses.html. Last accessed date on 2013.
41. Laarhoven PJM, Aarts EHL. *3D Simulated Annealing: Theory and Applications*. Dortrecht: Kluwer Academic Publisher, 1987.

Manuscript received Sept. 2, 2013, and revision received Dec. 29, 2013.